Graphene–dielectric composite metamaterials: evolution from elliptic to hyperbolic wavevector dispersion and the transverse epsilon-near-zero condition

Mohamed A. K. Othman
Caner Guclu
Filippo Capolino

Graphene–dielectric composite metamaterials: evolution from elliptic to hyperbolic wavevector dispersion and the transverse epsilon-near-zero condition

Mohamed A. K. Othman, Caner Guclu, and Filippo Capolino

University of California, Irvine,
Department of Electrical Engineering and Computer Science,
Irvine, California 92697
E-mail: fcapolino@uci.edu

Abstract. We investigated a multilayer graphene–dielectric composite material, comprising graphene sheets separated by subwavelength-thick dielectric spacer, and found it to exhibit hyperbolic isofrequency wavevector dispersion at far- and mid-infrared frequencies, allowing propagation of waves that would be otherwise evanescent in an isotropic dielectric. Electrostatic biasing was considered for tunable and controllable transition from hyperbolic to elliptic dispersion. We explored the validity and limitation of the effective medium approximation (EMA) for modeling wave propagation and cutoff of the propagating spatial spectrum due to the Brillouin zone edge. We reported that EMA is capable of predicting the transition of the isofrequency dispersion diagram under certain conditions. The graphene-based composite material allows propagation of backward waves under the hyperbolic dispersion regime and of forward waves under the elliptic regime. Transition from hyperbolic to elliptic dispersion regimes is governed by the transverse epsilon-near-zero (TENZ) condition, which implies a flatter and wider propagating spectrum with higher attenuation, when compared to the hyperbolic regime. We also investigated the wide-angle tunable transparency of the multilayer at that condition in contrast to other materials exhibiting ENZ phenomena. © *2013 Society of Photo-Optical Instrumentation Engineers (SPIE)* [DOI: 10.1117/1.JNP.7.073089]

1 Introduction

Hyperbolic metamaterial (HM) refers to a subcategory of uniaxially anisotropic metamaterial, that can be modeled by a diagonal permittivity tensor (in Cartesian co-ordinates) comprising entries with both positive and negative real parts. The realization of hyperbolic dispersion allows wave propagation over a wide spatial spectrum (infinite for an ideal HM), that would be evanescent in a common isotropic dielectric.[1] HMs are realized at optical frequencies using metal–dielectric multilayers,[2–4] or metallic nanowires,[5] and at terahertz and infrared frequencies using semiconductor–dielectric multilayers[6,7] or carbon nanotubes.[8] In multilayer HMs, the emergence of hyperbolic dispersion does not rely on any resonant feature, thus it poses a potential for broadband enhancement of the local density of states (LDOS),[9] subwavelength imaging,[10,11] and lensing.[12] Spontaneous emission rate of an emitter, as well as the radiative decay of dye molecules, is proportional to the LDOS,[11] hence it can be substantially enhanced in the proximity of an HM.[13,14] It was demonstrated in Ref. 2 that the power scattered by a passive nanosphere located in the proximity of a metal–dielectric HM is enhanced by orders of magnitude, while the HM absorbs most of the scattered power, opening a new Frontier in super absorber's designs based on near-fields transformation from evanescent to propagating regimes. A wide band absorption was devised in Ref. 15 using tilted carbon nanotubes. Multilayer HMs at optical frequencies take

advantage of the wide frequency band in which metals exhibit negative permittivity and support plasmonic modes.[2,3] At infrared frequencies, graphene as a tunable inductive layer constitutes a potential building block for multilayer HM realizations. Furthermore, tunability of HMs can be achieved using static fields to bias graphene.[16,17] It is a remarkable material with a wide operational frequency band starting from microwave regime,[18] through terahertz frequencies,[19] and optical frequencies.[20] Graphene was utilized in design of metasurfaces in many different applications, such as polarizers and absorbers[21,22] and cloaking devices.[23] In this paper, we investigate a graphene–dielectric multilayer material that shows promising properties as tunable HM at far- and mid-infrared frequencies, that was predicted to provide a large enhancement in the Purcell factor.[24,25] In that recent work,[25] the enhancement of emitted power by an electrically small emitter near the interface of graphene-based HM as well as the near-field absorption properties were developed using effective medium approximation (EMA) and transfer matrix methods, where the limitations and validity of EMA were established.[25] Here, we show how the wavevector dispersion diagram can be controlled and even transformed between hyperbolic and elliptic curves at mid- and far-infrared regime. Moreover, we demonstrate the design guidelines of the graphene-based HM in terms of the physical parameters for the purpose of engineering the evolution from hyperbolic to elliptic dispersion condition. In the last part of the paper we explore the transverse epsilon-near-zero (TENZ) condition, its relation to the dispersion diagram and the enhanced transparency of a thin film made of TENZ graphene–dielectric layers for TM waves with a wide range of incidence angle. The fabrication of the metamaterial comprising as few as 10 graphene–dielectric layers, which were shown to have characteristics that resembles those of a semi-infinite stack,[25] could be realized utilizing commercially available high-quality chemical-vapor-deposition-(CVD)-grown graphene monolayer on a transition metallic (Ni or Cu) foil[26,27] from which graphene can be transferred onto a SiO_2/Si substrate using an intermediate host such as a thermoplastic polymethyl-methacrylate for enhancing the transfer process efficiency.[28] This process is followed by depositing a thin film of SiO_2 or SiC on the graphene flake using CVD. However, it was shown that a graphene monolayer on SiO_2 can become highly disordered and increase scattering losses.[29] The transfer of few-layer graphene[26] on other compatible materials such as boron-nitride (h-BN) might be of interest toward realizing the metamaterial, since h-BN shares the same hexagonal structure with graphene.[30]

2 Effective Medium Analysis of Graphene–Dielectric Multilayers

Graphene is a one-atom-thick layer of a hexagonal arrangement of carbon atoms with a lattice constant of 0.264 nm, hence spatial dispersion effects introduced by graphene periodicity can be, in general, neglected at terahertz frequencies. Although the existence of extremely slow surface modes can trigger spatial dispersion effects,[18,31] those modes are essentially highly evanescent due to the periodicity of the multilayer structure studied here, as it will be shown in Sec. 3. Graphene is electrically modeled by the local isotropic sheet conductivity $\sigma = \sigma' + j\sigma''$ (assuming time-harmonic variation of $e^{j\omega t}$), which accounts for both interband and intraband contributions to the total electronic transport.[32,33] The sheet conductivity σ is computed by the Kubo formula,[34] which yields a function of frequency, chemical potential μ_c, phenomenological scattering rate Γ, and temperature T. Here, we assume for graphene $\Gamma = 0.33$ meV (using the same notation as in Ref. 34), which corresponds to a mean electron scattering time of about 1 ps, at room temperature $T = 300$ K. Graphene supports relatively low loss TM plasmonic modes[16] (dictated by the negative imaginary part of the surface conductivity $\sigma'' < 0$). As such, σ'', modeling the reactive response of graphene, plays a fundamental role in the manifestation of hyperbolic dispersion in multilayer graphene–dielectric materials, as described in the following. We aim at analyzing an infinite periodic multilayer structure depicted in Fig. 1 whose unit cell is composed of a graphene sheet and a dielectric layer of subwavelength thickness d and relative permittivity ϵ_d. A physical understanding of wave propagation in such multilayers with a subwavelength period can be established by using the EMA approach, which is a quasistatic or local approximation for metamaterials, often adopted for metal–dielectric multilayers.[2,3,31] According to EMA, the periodic multilayer is regarded as an anisotropic homogeneous medium with effective relative permittivity tensor $\underline{\epsilon}_{\text{eff}} = \epsilon_t(\hat{\mathbf{x}}\hat{\mathbf{x}} + \hat{\mathbf{y}}\hat{\mathbf{y}}) + \epsilon_z\hat{\mathbf{z}}\hat{\mathbf{z}}$, where the relative effective *transverse*
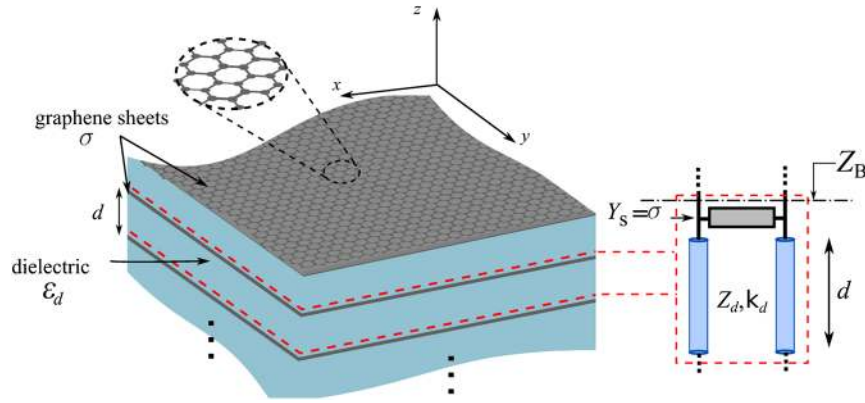
Fig. 1 Graphene–dielectric multilayer HM topology, modeled by a periodically loaded transmission line. The unit cell is indicated on the right and the graphene sheet is represented as a shunt admittance, and we denote the reference plane for evaluating the Bloch impedance. At far- and mid-infrared frequencies, TM^z waves exhibit hyperbolic isofrequency wavevector dispersion.

permittivity ϵ_t is found by averaging the transverse *effective* displacement current over the associated electric field in a unit cell. (Here, the effective displacement current is defined as a quantity that includes both displacement current in the dielectric slab and conduction current in the infinitesimally thin graphene sheet.) Then the relative effective permittivity parameter for transversely polarized field is

$$\epsilon_t = \epsilon_t{}' - j\epsilon_t'' = \epsilon_d - j\frac{\sigma}{\omega\epsilon_0 d}. \tag{1}$$

Since an individual graphene sheet is infinitesimally thin, the conduction current is always along the sheet, hence the permittivity experienced by z-directed electric field is not affected by graphene, leading to $\epsilon_z = \epsilon_d$. The relation in Eq. (1) implies that when the graphene sheet is adequately inductive, in particular when $\sigma'' < -\omega\epsilon_0\epsilon_d d$, we obtain $\epsilon_t' < 0$ and in turn the isofrequency wavevector dispersion is hyperbolic,[2] as demonstrated next. Let us consider plane waves propagating inside the metamaterial with the spatial dependence $e^{-j\mathbf{k}\cdot\mathbf{r}}$ where $\mathbf{k} = k_x\hat{\mathbf{x}} + k_y\hat{\mathbf{y}} + k_z\hat{\mathbf{z}}$ is the wavevector. A plane wave analysis is particularly useful in understanding the multilayer's response to sources because the radiation of a dipole inside or close to the metamaterial can be represented as a spatial spectral sum of plane waves. Due to the symmetry of the multilayer metamaterial with respect to the z-axis, we will use $k_t = \sqrt{k_x^2 + k_y^2}$ for denoting the transverse wavenumber component, and in the following, k_t is a real number k_t representing the spatial spectrum of TE^z (electric field transverse to z) and TM^z (magnetic field transverse to z) waves. The z-directed wavenumber $k_z = \beta_z - j\alpha_z$ can assume complex values modeling propagation and attenuation, accounting also for natural losses in the material constituents. Accordingly, the wavevector dispersion of TE^z and TM^z waves inside the effective medium is given as

$$k_z^2 = \epsilon_t k_0^2 - k_t^2, \qquad \text{TE}^z, \tag{2}$$

$$k_z^2 = \epsilon_t k_0^2 - \frac{\epsilon_t}{\epsilon_d}k_t^2, \qquad \text{TM}^z, \tag{3}$$

where $k_0 = \omega\sqrt{\mu_0\epsilon_0}$ is the wavenumber in free space. When the losses are neglected (i.e., if $\sigma' \to 0$) one would obtain purely real ϵ_t, hence k_z [obtained via Eqs. (2) and (3)] assumes either purely real values, denoting the propagating spectrum, or purely imaginary values, denoting the evanescent spectrum. In this lossless case, hyperbolic dispersion occurs when $\epsilon_t < 0$, and the HM uniaxial medium allows for propagation (i.e., k_z is a purely real number) of extraordinary waves (TM^z) with a large transverse wavenumber $k_t > \sqrt{\epsilon_d}k_0$; these waves with $k_t > \sqrt{\epsilon_d}k_0$ would be otherwise evanescent (i.e., k_z is purely imaginary) either in an isotropic dielectric with permittivity ϵ_d, or in a generic uniaxial anisotropic media with $\epsilon_t > 0$. This unusual phenomenon implies that high k_t spectrum emanating from sources, which would be evanescent in free

space, can be converted to propagating waves at HM interfaces. Ordinary waves (TE^z) are, however, evanescent for any k_t when $\epsilon_t < 0$. On the other hand, when $\epsilon_t > 0$ we have real k_z only for a limited spectrum of TM^z waves with $k_t < \sqrt{\epsilon_d}k_0$, which leads to the elliptic isofrequency wave-vector dispersion. Therefore the transition between hyperbolic to elliptic regimes is associated to the condition $\epsilon_t = 0$.

Instead, for realistic lossy cases, k_z is complex and the wavevector isofrequency dispersion becomes elliptic-like and hyperbolic-like (for $\epsilon_t' > 0$ and $\epsilon_t' < 0$, respectively), as shown in the examples in the next section. However, the interpretations regarding propagation of power are still valid provided that losses are relatively small, and we will show that moderate propagation losses are a major advantage of graphene-based HMs at far- and mid-infrared frequencies. When applying EMA, the dispersion relation $\beta_z - k_t$ is hyperbolic-like for $k_t > \sqrt{\epsilon_d}k_0$ when $\epsilon_t' < 0$, and it converges to the asymptote $|\beta_z| \approx |\epsilon_t' k_t / \epsilon_d|$ for large spatial wavenumber k_t, i.e., the $\beta_z - k_t$ dispersion becomes linear, with a slope of $|1 + \sigma''/(\omega\epsilon_0\epsilon_d d)|$.

To validate our EMA hypothesis, we obtain a more accurate representation of the wavevector dispersion relation by employing Bloch theory[35] for a periodically loaded transmission line whose unit cell is illustrated in Fig. 1. When each graphene sheet is modeled with a complex admittance $Y_s = \sigma = \sigma' + j\sigma''$, the dispersion relation for TM^z or TE^z waves in the periodic structure is cast in the form

$$\cos k_z d = \cos \kappa_d d + j\frac{Y_s}{2} Z_d \sin \kappa_d d, \tag{4}$$

where $\kappa_d = \sqrt{\epsilon_d k_0^2 - k_t^2}$ is the z-directed wavenumber of a wave inside the dielectric spacer, $Z_d^{TM} = \kappa_d/(\omega\epsilon_0\epsilon_d)$ and $Z_d^{TE} = \omega\mu_0/\kappa_d$ are the characteristic wave impedances for TM^z and TE^z waves, respectively. This relation in Eq. (4) is accurate for arbitrary d and k_t, i.e., accounts for transverse wavenumber dispersion. For the spectrum in which the dielectric layer's thickness is much smaller than the Bloch wavelength and the wavelength inside the dielectric itself ($|k_z d| \ll 1$, $|\kappa_d d| \ll 1$), we can apply the following small argument approximations $\cos x \approx 1 - x^2/2$ and $\sin x \approx x$, the dispersion relation in Eq. (4) simplifies to the one obtained via EMA in Eqs. (2) and (3) using the same definitions for ϵ_t and ϵ_z.[25] As we will discuss thoroughly in Sec. 3, Bloch theory proves that the propagating spectrum of TM^z waves is limited due to the periodicity, manifested by the Brillouin zone edge at which $\beta_z = \pm\pi/d$, and therefore the propagating spectrum in realistic HMs has an upper bound even in lossless cases. Nevertheless, the Brillouin zone edge (i.e., $\beta_z = \pm\pi/d$) is reached in general at the higher values of k_t, provided that the period d is extremely subwavelength.

In the following we report some aspects that demonstrate the merits of graphene-based HM: Graphene conductivity $\sigma = \sigma' + j\sigma''$ is tunable with chemical potential variation via electrostatic biasing, hence ϵ_t' is also tunable through negative or positive values at a fixed frequency. This implies a possible transition between hyperbolic to elliptic wavevector dispersion. The realization of HMs using graphene is also prone to graphene's frequency response. For instance, graphene sheets are mainly capacitive in mid- and near-infrared frequencies, because intraband contributions in graphene are dominant, and the TM^z surface modes on a single graphene layer become on the improper Riemann sheet.[16] On the other hand, at very low frequencies (tens of GHz), the interband conductivity dominates leading to high losses. Hence a proper frequency range for realizing hyperbolic dispersion extends from far-infrared up to low mid-infrared frequencies. Furthermore, the dielectric thickness also plays a role on the frequency range of HM design. As the dielectric thickness is increased, the frequency range of negative ϵ_t' shifts to lower frequencies which are undesirable due to significant losses in graphene. Moreover, thicker spacers require a larger biasing electrostatic potential between layers to achieve a moderate chemical potential level in graphene sheets. On the other hand, when considering smaller periods (in the range of several nanometers), it is expected that the graphene sheets are no longer electronically isolated for such quantum-scale interspacing, and a tight binding model for graphene layers must be taken into account in order to evaluate the conductivity of graphene sheets.[36,37] Therefore, for very small thicknesses, both EMA relation, reported in Eq. (3), and transfer matrix analysis must be modified to account for quantum tunneling between graphene sheets. In the next section, we will explore and provide illustrative examples for graphene-based HM designs in terms of frequency response, losses, and tunability and we will assess the validity of the EMA in predicting hyperbolic or elliptic dispersion regimes.

3 Hyperbolic and Elliptic Wavevector Dispersion

Let us consider the multilayer stack depicted in Fig. 1, that comprises graphene sheets and dielectric layers with $\epsilon_d = 2.2$ and thickness d. In our illustrations we only adopt positive values for graphene chemical potential owing to the assumed reciprocity in the multilayers, and consider a typical range for μ_c up to 0.5 eV in individual graphene sheets as suggested in Ref. 23. We plot in Fig. 2 the relative transverse permittivity $\epsilon_t = \epsilon_t' - j\epsilon_t''$ versus frequency for various chemical potential levels ($\mu_c = 0$, 0.25, and 0.5 eV) and dielectric thickness ($d = 100$, 50 nm). First we observe that the zero-crossing frequency of ϵ_t', where $\sigma'' = -\omega\epsilon_0\epsilon_d d$ is primarily defined by the period d and it can be tuned via the chemical potential; and as a result the frequency of transition between the hyperbolic and the elliptic dispersion regimes can be controlled. For example, when $d = 100$ nm (solid lines) in Fig. 2(a) we show that the frequency at which $\epsilon_t' = 0$ shifts from 6.6 to 27.5 THz by increasing the chemical potential from 0 to 0.5 eV. For $d = 50$ nm, similar control of the frequency at which $\epsilon_t' = 0$ is observed by varying μ_c. Moreover, when $\mu_c = 0$, we see that $\epsilon_t' = 0$ occurs at 8.7 THz for $d = 50$ nm, a higher frequency than the $d = 100$ nm case whose zero-crossing frequency is around 6.6 THz. Graphene sheets become capacitive at higher frequencies ($\sigma'' = 0$ denotes the transition from inductive to capacitive, for instance, $\sigma'' = 0$ at $\simeq26$ THz when $\mu_c = 0$ eV), however, its contribution to ϵ_t' becomes negligible because of both ω in the denominator of Eq. (1) and graphene conductivity saturates to $\pi e^2/(2\,h) \approx 60\,\mu S$ with a very small imaginary part, and hence ϵ_t' approaches ϵ_d.

We show a relative variation in ϵ_t'' when μ_c is increased, indicating a possible way to tune losses. Note that when the frequency dependent transverse permittivity ϵ_t' turns positive and becomes close to unity, satisfying $\sigma'' \approx \omega\epsilon_0 d(1 - \epsilon_d)$, for instance at 15.6 THz when $\mu_c = 0.25$ eV and $d = 100$ nm, a finite graphene–dielectric multilayer becomes almost transparent to TE^z and TM^z plane waves in free space with $k_t \ll k_0$, and all waves would travel with $k_z \approx k_0$, as seen from Eq. (3) when $\epsilon_t' \approx 1$.

In order to address some design considerations and tuning opportunities of graphene-based HM, we show in Fig. 3(a) and 3(b), the real and imaginary parts of ϵ_t as a colormap versus μ_c and d. We also indicate the $\epsilon_t' = 0$ contour denoting the transition between hyperbolic and elliptic dispersion regimes. The selection of d determines the range of chemical potential levels in which hyperbolic/elliptic dispersion occurs. For instance, when $d = 0.2\,\mu m$, a tuning range for hyperbolic dispersion starts at $\mu_c = 0.1$ eV, while for $d = 0.6\,\mu m$ it begins at $\mu_c = 0.35$ eV; this illustrates the need for thinner dielectric spacers due to the limitations on the chemical potential levels' adjustability, up to 0.5 eV in this paper. On the other hand, the choice of a thinner dielectric spacer, i.e., smaller d, effectively induces higher ϵ_t'', so the losses embodied in ϵ_t'' are larger at the same frequency and bias. For example, when $d = 0.1\,\mu m$, $\epsilon_t'' \simeq 0.4$ but when $d = 0.4\,\mu m$ we notice that $\epsilon_t'' \simeq 0.2$, with larger negative ϵ_t' in the former case than in the latter. Nonetheless, a thin dielectric spacer allows feasible biasing by standard values of static potential.[21] This demonstrates a basic trade-off in graphene–dielectric HM design, between the tuning ranges, losses, and effective negative values of ϵ_t', and leads to a broad interpretation of the respective wavevector dispersion as described next.
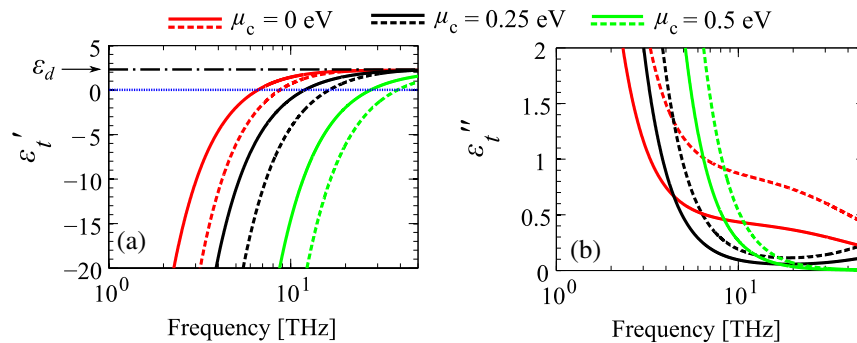

Fig. 2 Real and imaginary parts of the effective relative transverse permittivity $\epsilon_t = \epsilon_t' - j\epsilon_t''$ for graphene-based multilayer HM for two possible designs with $d = 100$ nm (solid lines) and $d = 50$ nm (dashed lines).
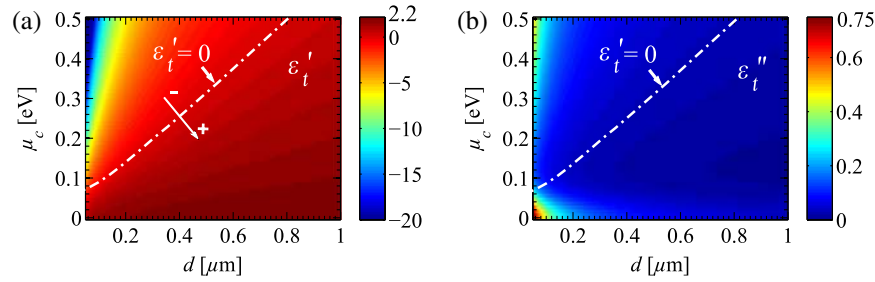
Fig. 3 Contour plot exploring the tuning capabilities of ϵ_t for graphene-based HM via chemical potential μ_c and dielectric thickness d at 10 THz.

The TM^z wavevector dispersion diagrams according to EMA Eq. (3) and Bloch theory for the multilayered medium Eq. (4) are shown in Fig. 4. Here, we report one of the two solutions of Eqs. (3) and (4) for $k_z = \beta_z - j\alpha_z$ that corresponds to a wave whose Poynting vector is directed toward the $+z$-direction, noting that the other root $-k_z$ is also a solution of Eqs. (3) and (4), not reported for symmetry reasons. Accordingly, the attenuation constant α_z has a positive sign associated to the field decay (due to possible losses) along the $+z$-direction. On the other hand, for the hyperbolic regime one observes $\beta_z < 0$ indicating backward wave propagation because it satisfies the backward wave condition $\beta_z \alpha_z < 0$ as explained in Ref. 38, for $k_t > \sqrt{\epsilon_d} k_0$. In general, for the elliptic case, when $k_t < \sqrt{\epsilon_d} k_0$ the valid $k_z = \beta_z - j\alpha_z$ solution with positive α_z is the one with $\beta_z > 0$, indicating that waves under the elliptic dispersion regime are forward waves because they satisfy the condition $\beta_z \alpha_z > 0$. In Fig. 4(c) and 4(d), we show the dispersion diagrams in a much wider spatial spectrum than in Fig. 4(a) and 4(b) for the same cases. In the reported cases, all with $d = 100$ nm, β_z curves in Fig. 4 keep either an overall hyperbolic or elliptic shape due to limited losses. When $\mu_c = 0$ eV (and correspondingly $\epsilon'_t > 0$) the medium exhibits elliptic dispersion, moreover β_z is nonzero for $k_t > \sqrt{\epsilon_d} k_0$ where α_z exhibits a dramatic increase, i.e., waves become mostly evanescent. On the other hand, when $\mu_c = 0.25$ or 0.5 eV,
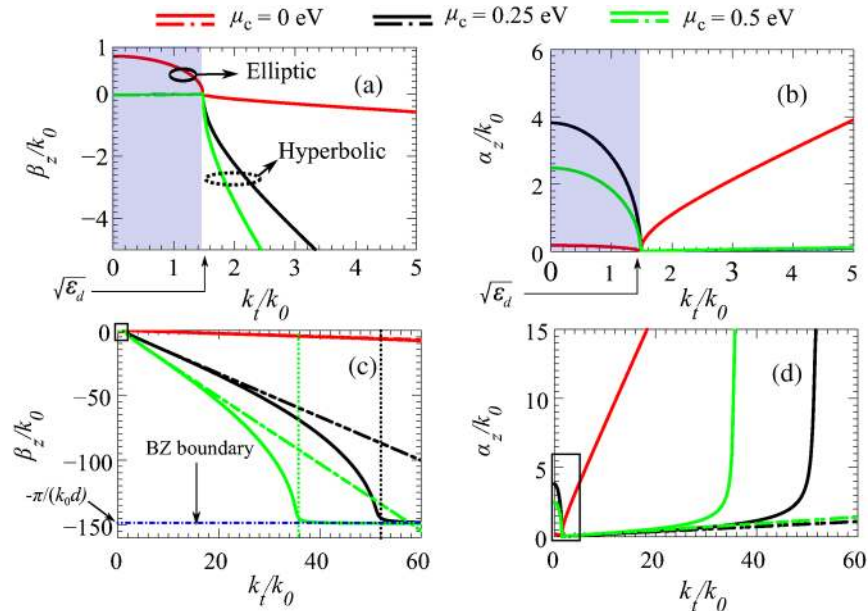

Fig. 4 Wavevector dispersion diagram of (a) β_z and (b) α_z versus k_t (both normalized by k_0) at 10 THz and $d = 100$ nm. In (c) and (d) a wider spatial spectrum of the wavevector dispersion is provided in order to identify k_t values, where β_z approaches the Brillouin zone edge ($\beta_z = -\pi/d$) denoted by a horizontal dotted line in (c). This happens when $k_t \approx 52k_0$ and $k_t \approx 38k_0$ for $\mu_c = 0.25$ eV and $\mu_c = 0.5$ eV, respectively. Calculations are based on both EMA (dash-dotted lines) and Bloch theory (solid lines).
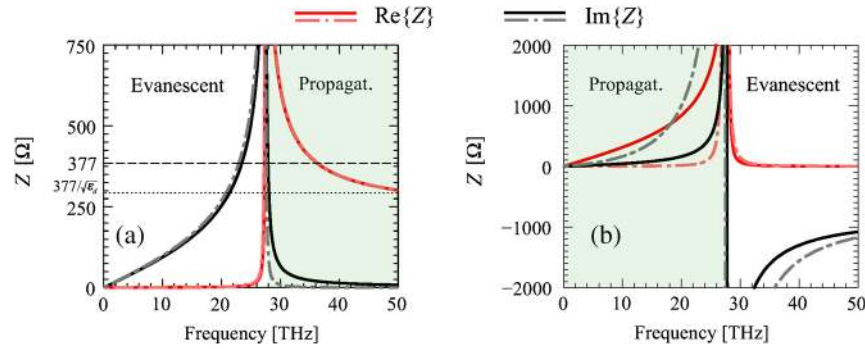
Fig. 5 Real and imaginary parts of the Bloch (solid lines) and effective (dashed lines) impedance of graphene–dielectric multilayers with $d = 100$ nm when $\mu_c = 0.5$ eV for (a) $k_t = 0$ and (b) $k_t = 5k_0$.

one has $\epsilon'_t < 0$ leading to the hyperbolic dispersion. We emphasize that EMA is fully capable of predicting the hyperbolic and elliptic wavevector dispersion regimes in the spatial spectrum reported in Fig. 4(a) and 4(b) in perfect agreement with the Bloch wavenumber. In a much wider range of the spatial spectrum k_t as in Fig. 4(c) and 4(d) the EMA-based normalized wavenumber β_z/k_0 starts to deviate from Bloch theory. Bloch theory predicts the band edge where β_z approaches $-\pi/d$ and α_z exhibits a dramatic increase, denoting a bandgap. However, EMA assumes infinite growth of β_z/k_0 following the asymptotic linearized $\beta_z - k_t$ relation, given by $\beta_z \approx -\epsilon'_t k_t / \epsilon_d$ when $k_t \gg k_0$. For higher negative values of ϵ'_t (corresponding to higher μ_c) the Brillouin zone band edge is met at smaller k_t due to steeper $\beta_z - k_t$ curves, as seen from Fig. 4(c) ($\epsilon'_t \simeq -1$ and $\epsilon'_t \simeq -11$ for $\mu_c = 0.25$ and 0.5 eV). Although the effective permittivity parameters are important for fast characterization of graphene–dielectric composites and providing physical interpretation of the evolution from elliptic to hyperbolic dispersion, they do not account for transverse wavenumber dispersion.[31,39] Accordingly, EMA predicts an indefinite propagating spatial spectrum in HMs (that is indeed limited by Brillouin zone edge according to Bloch model), and consequently overestimates the LDOS and the near-field power absorption in HMs as already discussed in Refs. 2–4, 25.

We provide in Fig. 5 both the Bloch impedance of graphene–dielectric multilayers at the reference plane shown in Fig. 1, with $d = 100$ nm. In addition, we report the effective wave impedance of the metamaterial obtained via EMA for TM^z plane wave, $Z_{\mathrm{eff}} = k_z/(\omega \epsilon_0 \epsilon_t)$ where k_z is evaluated using Eq. (3) (see Ref. 40). The two impedances are close to each other for $k_t = 0$ case [Fig. 5(a)] whereas for $k_t = 5k_0$ the effective impedance shows a noticeable difference for both real and imaginary parts from the Bloch calculations. Nonetheless, the effective impedance provides a good prediction regarding the transition frequency between propagating and evanescent spectra. Moreover, we notice that the real part of the impedance is negligible at low frequencies in Fig. 5(a), whereas it peaks at the frequency where $\epsilon'_t = 0$. From Fig. 6(a) one can see that after ϵ'_t turns positive, the impedance becomes dominantly real, with a relatively small reactive part, owing to the presence of a mainly propagating plane wave in elliptic dispersion regime for $k_t = 0$. On the contrary for $k_t = 5k_0$ case, at lower frequencies, the wave propagates in the hyperbolic dispersion regime while having $\epsilon'_t < 0$, and the
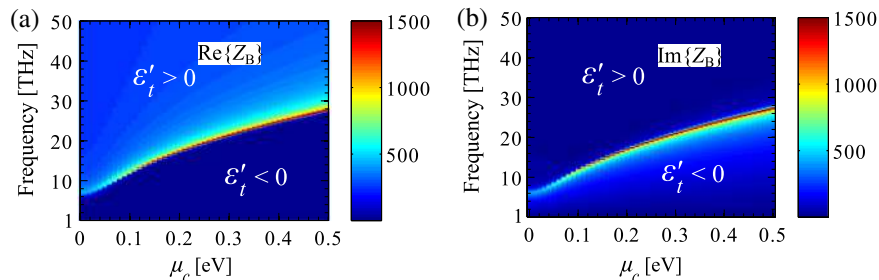

Fig. 6 (a) Real and (b) imaginary parts of the Bloch impedance for $d = 100$ nm and $k_t = 0$.

impedance real part is relatively large, as depicted in Fig. 5(b), whereas the impedance becomes almost purely reactive after ϵ'_t turns positive, denoting a mainly evanescent wave. At higher frequencies, the impedance for $k_t = 0$ case becomes matched to free space at ≈ 37 THz at which $\epsilon'_t \approx 1$ as shown in Fig. 6(a). At much higher frequency ranges, the impedance approaches the impedance in isotropic lossless dielectric where $\epsilon_t \approx \epsilon_d$ in both Fig. 5(a) and 5(b). For clarification, we report the Bloch impedance as a color plot showing the dependance on frequency and chemical potential in Fig. 6, where the impedance peaking is observed as a clear manifestation of the TENZ condition, as will be demonstrated in Sec. 4. Based on the conclusions in Ref. 25, in order to guarantee the validity of EMA for each spectral component of propagating plane waves with $k_t < k_0$, the dielectric thickness should be electrically small, i.e., $d < 0.02\lambda_0$ for accurate representation of the impedance and wavevector using the homogenized model derived above.

We report in Fig. 7 the frequency dependance of the quantity $|\beta_z/\alpha_z|$ where α_z and β_z are calculated by Bloch theory, for graphene–dielectric multilayers with $d = 100$ nm. The ratio $|\beta_z/\alpha_z|$ constitutes a figure of merit for understanding if a wave is mainly propagating or attenuating. The horizontal white dash-dotted line marks the transition frequency from hyperbolic to elliptic dispersion (the latter occurring always above the transition frequency) and the transition happens when the real part ϵ'_t crosses zero and turns positive causing the elliptic regime. For $k_t < \sqrt{\epsilon_d}k_0$, β_z is relatively very small compared to α_z, which implies mainly evanescent spectrum (purely evanescent in the absence of losses), for hyperbolic dispersion frequencies $\omega < -\sigma''/(\epsilon_0\epsilon_d d)$. However, for $k_t > \sqrt{\epsilon_d}k_0$, wavevector dispersion has a hyperbolic-like shape, with attenuation α_z moderately low (and slightly increasing as seen in Fig. 7) due to the losses in graphene, and therefore $|\beta_z/\alpha_z|$ exhibits an overall increase where it reaches a maximum value $\simeq 130$ as in $\mu_c = 0.5$ eV yielding a wide propagating spectrum $\sqrt{\epsilon_d} < k_t/k_0 < 40$ at 10 to 20 THz. Notice that for even larger k_t, the propagation constant β_z tends to $-\pi/d$ while α_z experiences an abrupt increase, as shown in Fig. 4(d), denoting the beginning of a strong evanescent spectrum. In the elliptic dispersion regime, occurring at higher frequencies such that $\omega > -\sigma''/(\epsilon_0\epsilon_d d)$, the trend for β_z and α_z is reversed. Elliptic dispersion arises at 6.6 THz for $\mu_c = 0$ eV, as depicted in Fig. 7, and the propagating spectrum with $k_t < \sqrt{\epsilon_d}k_0$ is allowed in the composite multilayer. For higher chemical potentials, for example $\mu_c = 0.5$ eV, hyperbolic wavevector dispersion is supported for frequencies up to 27.4 THz, and the dispersion becomes elliptical thereafter. Notice that at frequencies less than 1 THz, waves poorly propagate due to higher losses in graphene sheets, i.e., wave propagation has a low figure of merit. On the other hand, elliptic dispersion regime, occurring for frequencies greater than 30 THz, has small attenuation constant for $k_t < \sqrt{\epsilon_d}k_0$ due to relatively low loss in graphene, and thus a high figure of merit $|\beta_z/\alpha_z| > 150$. Note that the lowest operational frequency for hyperbolic dispersion regime with high $|\beta_z/\alpha_z|$ is limited by graphene losses, whereas the highest frequency is tunable by the chemical potential.

We now examine how the figure of merit $|\beta_z/\alpha_z|$ varies versus the transverse wavenumber k_t, assuming different design values for the dielectric spacing d. In Fig. 8(a) we observe $|\beta_z/\alpha_z|$ at 10 THz varying d, for $\mu_c = 0$ eV, where only elliptic dispersion regime is observed for any
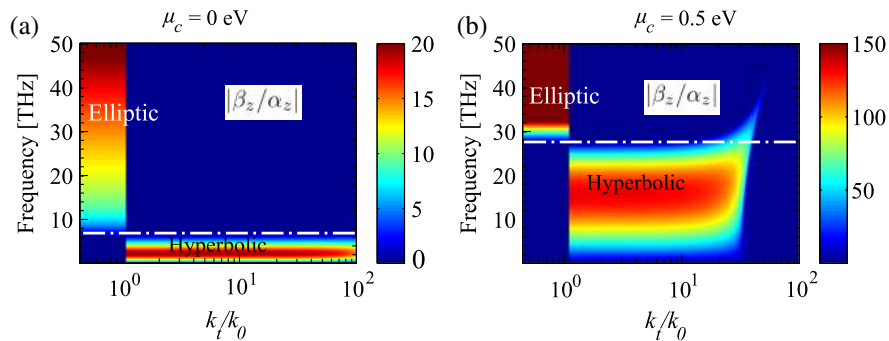

Fig. 7 The figure of merit $|\beta_z/\alpha_z|$ versus frequency and spatial wavenumber k_t, for both hyperbolic and elliptic regimes. Two chemical potential levels are considered: (a) $\mu_c = 0$ eV and (b) $\mu_c = 0.5$ eV.
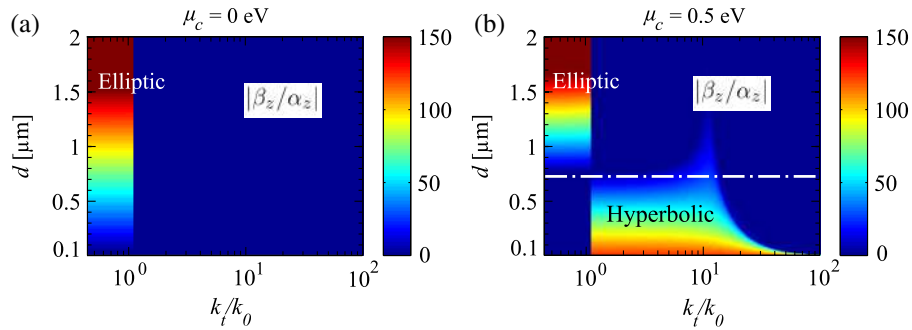
Fig. 8 The figure of merit $|\beta_z/\alpha_z|$ versus dielectric thickness d and spatial wavenumber k_t, at 10 THz, for both hyperbolic and elliptic regimes. Two chemical potential levels are considered: (a) $\mu_c = 0$ eV and (b) $\mu_c = 0.5$ eV.

thickness d considered. However, hyperbolic dispersion is supported when appropriate chemical potential is achieved, as shown in Fig. 8(b) for $\mu_c = 0.5$ eV. In this latter case, when $d = 1$ μm, TM^z waves are mainly evanescent for large transverse wavenumber $k_t > \sqrt{\epsilon_d}k_0$, irrespective of the chemical potential levels reported here. Consequently, a typical dielectric thickness in the range of 50 to 100 nm is deemed appropriate to utilize in graphene–dielectric multilayers for tunable HM designs.

4 Transverse Epsilon-Near-Zero Condition

Finally, we describe an interesting frequency region at which ϵ_t' changes sign and it assumes values very close to zero. We denote this regime as TENZ, which is manifested under the condition $\sigma'' \approx -\omega\epsilon_0\epsilon_d d$, i.e., when a graphene sheet's inductive susceptance compensates for the small capacitive susceptance of each dielectric layer. We show in Fig. 9(a) and 9(b), the level of biasing potential (μ_c) required to achieve the TENZ condition at a given frequency and the corresponding ϵ_t'', respectively. We note that the required bias voltage for TENZ at a certain frequency decreases for thinner unit cells, i.e., smaller d, however, losses become larger due to increased graphene sheet density, especially at low frequencies. For example when $d = 50$ nm, we require μ_c to be tuned to 0.1 eV in order to achieve the TENZ condition at 15 THz, and we have $\epsilon_t'' \approx 0.1$, whereas if the metamaterial is designed with $d = 200$ nm, the amount of bias required to realize TENZ condition at the same frequency is about 0.2 eV and the losses are lower $\epsilon_t'' \approx 0.02$. In view of such observations one can easily identify the tuning ranges and show that for smaller unit cell thickness the tuning range is larger but one must tolerate the losses in such design.
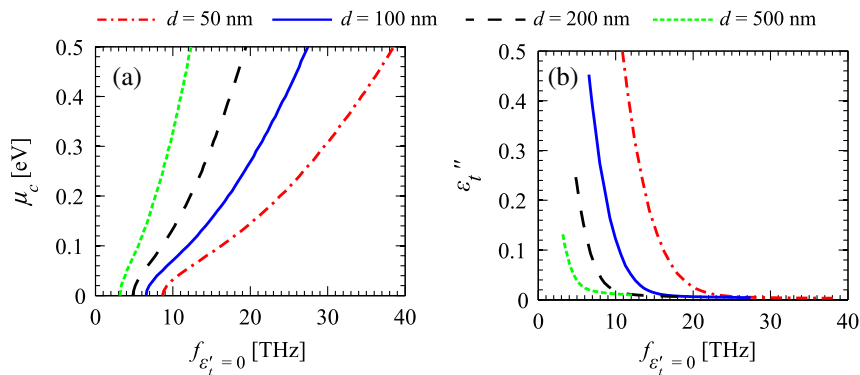

Fig. 9 (a) The zero-crossing frequency of ϵ_t' evaluated according to EMA $f_{\epsilon_t'=0} = \sigma''/(2\pi e_0 e_d d)$ varying the chemical potential, for various thicknesses d. (b) Imaginary part of the transverse permittivity ϵ_t'' evaluated at $f_{\epsilon_t'=0}$.

When considering wave propagation at that particular condition, and if losses are to be neglected without compromising the generality of the conclusions, the quasistatic approximation derived from EMA Eq. (3) reveals a $\beta_z - k_t$ dispersion relation with a very small slope, i.e., the dispersion curve is almost flat. However, at higher k_t the EMA approximations become inaccurate, and β_z grows until it reaches the Brillouin zone edge $-\pi/d$. The accurate wavevector dispersion of TM^z waves according to Bloch theory, using Eq. (4) and $Z_d^{\text{TM}} = \kappa_d/(\omega\epsilon_0\epsilon_d)$, is given by

$$\cos k_z d = \cos \kappa_d d + j \frac{(\sigma' + j\sigma'')}{2} \frac{\kappa_d}{\omega\epsilon_0\epsilon_d} \sin \kappa_d d. \tag{5}$$

The condition $\epsilon_t' \approx 0$ is satisfied when $\omega\epsilon_0\epsilon_d d \approx -\sigma''$, and it leads to

$$\cos k_z d \approx \cos \kappa_d d + \frac{\kappa_d d}{2} \sin \kappa_d d + j \left| \frac{\sigma'}{2\sigma''} \right| \kappa_d d \sin \kappa_d d. \tag{6}$$

This latter dispersion equation is further simplified under the small argument approximation, $|\kappa_d d| \ll 1$ as

$$\cos k_z d \approx 1 + j(\kappa_d d)^2 \left| \frac{\sigma'}{2\sigma''} \right| + O(|\kappa_d d|^4). \tag{7}$$

The imaginary term in Eq. (7) is negligible since $|(\kappa_d d)^2 \sigma'/2\sigma''| \ll 1$ for graphene–dielectric multilayer with a subwavelength period, and, therefore, one simply obtains $k_z \approx 0$, far enough from the Brillouin zone edge. Therefore, the TENZ condition $\epsilon_t' \approx 0$, implies a flat isofrequency dispersion diagram with small k_z over a wide range of k_t. We report in Fig. 10(a) and 10(b) the isofrequency wavevector dispersion at four different frequencies, at which we show hyperbolic dispersion (10 THz with $\epsilon_t \simeq -1.01 - j0.09$), elliptic dispersion (15 THz with $\epsilon_t \simeq 0.84 - j0.05$), and the TENZ transitional state (at 11.9 and 12 THz, with $\epsilon_t \simeq -0.001 - j0.075$ and $\epsilon_t \simeq 0.028 - j0.072$, respectively), where both β_z and α_z for all cases are normalized by k_0. In Fig. 10(a) one can observe that the slope of the $\beta_z - k_t$ dispersion is reduced when $|\epsilon_t'|$ is much smaller than unity, as also predicted analytically in Eq. (7), still preserving limited values of the attenuation constant α_z. Note that the elliptic regime (at 15 THz) also shows a very low slope of the $\beta_z - k_t$ dispersion, however the attenuation constant α_z is large, because waves are mainly evanescent for large k_t. Fig. 10(a) shows that the TENZ regimes are responsible for almost flat propagation constant ($|\beta_z/k_0| < 1$) up to $k_t \simeq 10k_0$, with a moderately low attenuation constant α_z. However, for larger k_t, we observe that β_z experiences a sharp increase toward the Brillouin zone edge, together with an increase of the attenuation constant α_z. In Fig. 10(b) we observe that the attenuation constant exhibits significant difference for
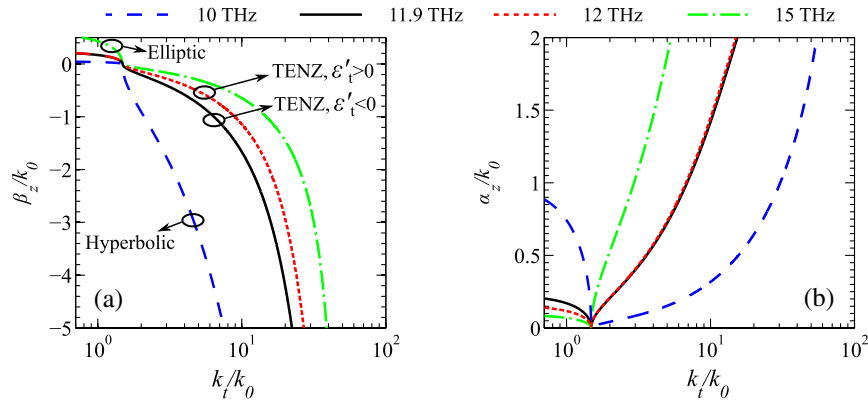

Fig. 10 Isofrequency wavevector dispersion in the TENZ, hyperbolic, and elliptic regimes, showing both (a) β_z and (b) α_z calculated by Bloch theory at four different frequencies (10, 11.9, 12, 15 THz), when $\mu_c = 0.1$ eV.

HM and TENZ regimes that requires some important consideration. Although the two TENZ cases have smaller ϵ_t'' than the hyperbolic one (at 10 THz), they experience a higher attenuation than HM case for $k_t > \sqrt{\epsilon_d}k_0$, whereas the opposite relation is valid for $k_t < \sqrt{\epsilon_d}k_0$. Therefore, we can observe the two trends: on one hand TENZ allows flatter $\beta_z - k_t$ relation and a wider k_t spectrum than a fully hyperbolic regime, and on the other hand the hyperbolic regime exhibits smaller attenuation constant than the TENZ cases. Note also that the TENZ is a transitional state toward elliptic dispersion, at which the attenuation α_z becomes even higher for $k_t > \sqrt{\epsilon_d}k_0$, and forward waves ($\beta_z \alpha_z > 0$) can propagate for $k_t < \sqrt{\epsilon_d}k_0$ with low attenuation constant.

It has been shown in Refs. 41, 42 that isotropic epsilon-near-zero (IENZ) material inside a waveguide supporting TE modes is able to tunnel electromagnetic waves. Here, we elaborate on TENZ materials at far- and mid-infrared frequencies designed using graphene–dielectric multilayers and explore their capabilities of tunneling electromagnetic waves.[43] Consider an electrically thin slab of thickness h made by either a TENZ ($\epsilon_t \approx 0$, $\epsilon_z \neq 0$) or an IENZ ($\epsilon_t = \epsilon_z = \epsilon_r \approx 0$) material in free space. Under TE^z wave incidence, TENZ and IENZ slabs provide an identical response and the reflection from such slabs can be set arbitrarily small by decreasing their thickness, as reported in Ref. 44. However, for TM^z oblique plane waves impinging on a lossless IENZ semi-infinite material, total reflection occurs for angles greater than the critical angle $k_t^c/k_0 = \sin\theta_i^c = \sqrt{\epsilon_r} \approx 0$. For an electrically thin IENZ slab, transmission of TM^z plane wave takes place for small angles of incidence ($0 < \theta_i < \theta_i^c$, where θ_i^c is considerably small) due to evanescent waves exhibiting frustrated multiple reflections at the slab interfaces. By including the effect of losses in IENZ slabs, absorption and local electric field enhancement were reported for specific incident angles $\theta_i > \theta_i^c$ in Ref. 45. Instead, we provide here the TM^z reflection and transmission coefficients (R_{TM}^{TENZ} and T_{TM}^{TENZ}) for a thin TENZ slab

$$R_{TM}^{TENZ} = \frac{\zeta}{2Z_0 + \zeta}, \quad T_{TM}^{TENZ} = \frac{2Z_0}{2Z_0 + \zeta}, \tag{8}$$

where

$$\zeta = \frac{jh(k_0^2 - k_t^2/\epsilon_z)}{\omega\epsilon_0}, \quad Z_0 = \frac{\sqrt{k_0^2 - k_t^2}}{\omega\epsilon_0}. \tag{9}$$

Therefore upon having a thin slab of TENZ material, ζ can be made small enough (due to the existence of finite, nonvanishing ϵ_z) in order to observe complete transmission for oblique TM^z waves with a wide range of incidence angles. This is in contrast to what happens for the IENZ case with ϵ_z assuming near-zero values, which implies that transmission only occurs around $k_t \approx 0$. We show in Fig. 11 the reflection and transmission at 37 THz, by a TENZ material with $\epsilon_t = -0.001$ and $\epsilon_z = 2.2$, and by an IENZ material with $\epsilon_r = -0.001$, assuming in both cases negligible losses. It is clear that the IENZ material exhibits a very narrow transmission
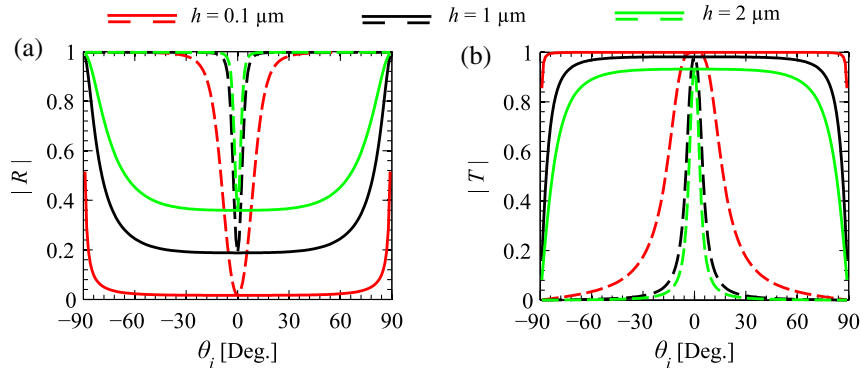

Fig. 11 Different characteristics of TM^z plane wave (a) reflection and (b) transmission from a thin slab made by a TENZ material (solid lines) and IENZ material (dashed lines) at 37 THz. Material losses in this example are assumed negligible. The TENZ material exhibits much wider and flatter parameters varying angle of incidence than the IENZ material.
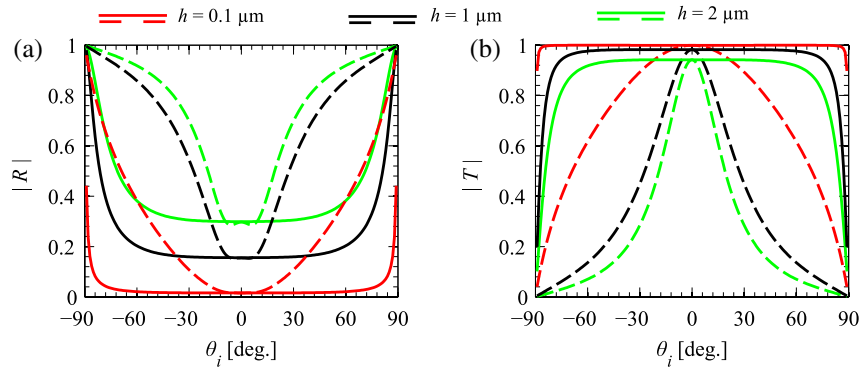
Fig. 12 TM^z plane wave (a) reflection and (b) transmission from a slab made by graphene–dielectric layers with $d = 50$ nm and $h = Nd$ (solid lines, using transfer matrix analysis) and an isotropic InAsSb slab of thickness h (dashed lines) at 37 THz.

around $\theta_i \approx 0°$ only due to evanescent waves (permittivity has a negative value) tunneling through the subwavelength slab,[43,45] and the transmission window dramatically diminishes as ϵ_r approaches zero or h increases, in accordance with the trend observed in Ref. 44. On the contrary, the TENZ slab exhibits large and stable transmission over a wide range of incidence angles, inherently complying with the flat wavevector dispersion relation in Eq. (7). Also, one should point out that the TM^z transmission in TENZ materials occurs up to much larger incidence angles than TE^z transmission, which is identical to an IENZ slab's TE transmission discussed in Ref. 44. In principle the different properties illustrated in the preceding simple example reveal the advantage of TENZ material over conventional IENZ material in enhancing transmission under oblique TM^z plane wave incidence. For a more practical comparison, we report in Fig. 12 the transmission and reflection for two possible TENZ and IENZ materials at mid-infrared. We consider a TENZ made of graphene–dielectric multilayer biased with $\mu_c = 0.5$ eV, accounting for losses, and having total thickness of $h = Nd$ where $d = 50$ nm, at 37 THz. Under these conditions EMA estimates $\epsilon_t \approx -0.001 - j0.031$ as seen from Fig. 2. The IENZ material is assumed to be a heavily n-doped InAsSb semiconductor,[46] which is engineered via doping to exhibit low loss IENZ in this frequency range, i.e., $\epsilon_{InAsSb} \approx -0.0001 - j0.038$ at ≈ 37 THz (experimentally shown in Ref. 46). In graphene-based TENZ material we observe a stable transmission with respect to the angle of incidence, and it is not affected much by losses in graphene as deduced from the comparison of the lossy case in Fig. 12 and the lossless case in Fig. 11. The InAsSb thin slab, however, exhibits a narrow angular range of transmission with higher sensitivity to losses, i.e., as the imaginary part of ϵ_r is increased, angular transmission is slightly broadened, especially as h increases. This indicates an advantage of using the graphene-based TENZ materials in tuning and enhancing TM^z plane wave transmission for wide angles of incidence. On the other hand, losses in natural materials or engineered metamaterials that exhibit IENZ behavior degrades the performance considerably, and may require integration of gain materials as in Ref. 45.

5 Conclusion

We have reported an HM implementation at far- and mid-infrared frequencies that comprises graphene–dielectric layers, and showed that EMA describes the hyperbolic wavevector dispersion as well as the transition to elliptic regime for specific conditions. Hyperbolic dispersion have manifested mainly at far-infrared frequencies, where we have investigated the propagating spectrum properties and discussed the effect of losses. We also showed that hyperbolic and elliptic dispersion regimes are associated to backward and forward wave propagation, respectively. We have explored the tuning opportunities and design considerations of the structure, as well as the translation from hyperbolic to elliptic wavevector dispersion, and demonstrated a transitional state, TENZ, at which the wavevector dispersion diagram becomes very

flat. Furthermore, we have demonstrated that a thin slab made by a TENZ material becomes transparent to both TE^z and TM^z plane wave, with the interesting characteristic that the transmission and reflection of TM^z waves are stable with respect to the incident angle, in contrast to what happens in conventional IENZ materials. This property can be utilized in designing ultra-thin films for tunable infrared applications.

References

1. D. R. Smith and D. Schurig, "Electromagnetic wave propagation in media with indefinite permittivity and permeability tensors," *Phys. Rev. Lett.* **90**(7), 077405 (2003), http://dx.doi.org/10.1103/PhysRevLett.90.077405.
2. C. Guclu, S. Campione, and F. Capolino, "Hyperbolic metamaterial as super absorber for scattered fields generated at its surface," *Phys. Rev. B* **86**(20), 205130 (2012), http://dx.doi.org/10.1103/PhysRevB.86.205130.
3. O. Kidwai, S. V. Zhukovsky, and J. E. Sipe, "Effective-medium approach to planar multilayer hyperbolic metamaterials: strengths and limitations," *Phys. Rev. A* **85**(5), 053842 (2012), http://dx.doi.org/10.1103/PhysRevA.85.053842.
4. O. Kidwai, S. V. Zhukovsky, and J. E. Sipe, "Dipole radiation near hyperbolic materials: applicability of effective-medium approximation," *Opt. Lett.* **36**(13), 2530–2532 (2011), http://dx.doi.org/10.1364/OL.36.002530.
5. E. Narimanov et al., "Darker than black: radiation-absorbing metamaterial," in *The Conference on Lasers and Electro-Optics(CLEO)/The International Quantum Electronics Conference(QELS)*, p. QPDA6, OSA, Washington, DC (2010).
6. C. Rizza et al., "Terahertz active spatial filtering through optically tunable hyperbolic metamaterials," *Opt. Lett.* **37**(16), 3345–3347 (2012), http://dx.doi.org/10.1364/OL.37.003345.
7. G. Naik and A. Boltasseva, "Semiconductors for plasmonics and metamaterials," *Phys. Status Solidi (RRL)* **4**(10), 295–297 (2010), http://dx.doi.org/10.1002/pssr.201004269.
8. I. Nefedov and S. Tretyakov, "Ultrabroadband electromagnetically indefinite medium formed by aligned carbon nanotubes," *Phys. Rev. B* **84**(11), 113410 (2011), http://dx.doi.org/10.1103/PhysRevB.84.113410.
9. Z. Jacob et al., "Engineering photonic density of states using metamaterials," *Appl. Phys. B* **100**(1), 215–218 (2010), http://dx.doi.org/10.1007/s00340-010-4096-5.
10. K. J. Webb and M. Yang, "Subwavelength imaging with a multilayer silver film structure," *Opt. Lett.* **31**(14), 2130–2132 (2006), http://dx.doi.org/10.1364/OL.31.002130.
11. C. L. Cortes et al., "Quantum nanophotonics using hyperbolic metamaterials," *J. Opt.* **14**(6), 063001 (2012), http://dx.doi.org/10.1088/2040-8978/14/6/063001.
12. J. Bénédicto, E. Centeno, and A. Moreau, "Lens equation for flat lenses made with hyperbolic metamaterials," *Opt. Lett.* **37**(22), 4786–4788 (2012), http://dx.doi.org/10.1364/OL.37.004786.
13. J. Kim et al., "Improving the radiative decay rate for dye molecules with hyperbolic metamaterials," *Opt. Express* **20**(7), 8100–8116 (2012), http://dx.doi.org/10.1364/OE.20.008100.
14. H. N. S. Krishnamoorthy et al., "Topological transitions in metamaterials," *Science* **336**(6078), 205–209 (2012), http://dx.doi.org/10.1126/science.1219171.
15. S. M. Hashemi and I. S. Nefedov, "Wideband perfect absorption in arrays of tilted carbon nanotubes," *Phys. Rev. B* **86**(19), 195411 (2012), http://dx.doi.org/10.1103/PhysRevB.86.195411.
16. G. W. Hanson, A. B. Yakovlev, and A. Mafi, "Excitation of discrete and continuous spectrum for a surface conductivity model of graphene," *J. Appl. Phys.* **110**(11), 114305 (2011), http://dx.doi.org/10.1063/1.3662883.
17. A. Vakil and N. Engheta, "Transformation optics using graphene," *Science* **332**(6035), 1291–1294 (2011), http://dx.doi.org/10.1126/science.1202691.
18. G. Lovat, "Equivalent circuit for electromagnetic interaction and transmission through graphene sheets," *IEEE Trans. Electromagn. Compat.* **54**(1), 101–109 (2012), http://dx.doi.org/10.1109/TEMC.2011.2169072.

19. M. Tamagnone et al., "Analysis and design of terahertz antennas based on plasmonic resonant graphene sheets," *J. Appl. Phys.* **112**(11), 114915 (2012), http://dx.doi.org/10.1063/1.4768840.

20. S. Thongrattanasiri, F. H. L. Koppens, and F. J. Garcia de Abajo, "Complete optical absorption in periodically patterned graphene," *Phys. Rev. Lett.* **108**(4), 047401 (2012), http://dx.doi.org/10.1103/PhysRevLett.108.047401.

21. A. Fallahi and J. Perruisseau-Carrier, "Design of tunable biperiodic graphene metasurfaces," *Phys. Rev. B* **86**(19), 195408 (2012), http://dx.doi.org/10.1103/PhysRevB.86.195408.

22. A. Fallahi and J. Perruisseau-Carrier, "Manipulation of giant faraday rotation in graphene metasurfaces," *Appl. Phys. Lett.* **101**(23), 231605–231605 (2012), http://dx.doi.org/10.1063/1.4769095.

23. P.-Y. Chen and A. Alu, "Atomically thin surface cloak using graphene monolayers," *ACS Nano* **5**(7), 5855–5863 (2011), http://dx.doi.org/10.1021/nn201622e.

24. I. V. Iorsh et al., "Hyperbolic metamaterials based on multilayer graphene structures," *Phys. Rev. B* **87**(7), 075416 (2013), http://dx.doi.org/10.1103/PhysRevB.87.075416.

25. M. A. K. Othman, C. Guclu, and F. Capolino, "Graphene-based tunable hyperbolic metamaterials and enhanced near-field absorption," *Opt. Express* **21**(6), 7614–7632 (2013), http://dx.doi.org/10.1364/OE.21.007614.

26. A. Reina et al., "Large area, few-layer graphene films on arbitrary substrates by chemical vapor deposition," *Nano Lett.* **9**(1), 30–35 (2009), http://dx.doi.org/10.1021/nl801827v.

27. X. Li et al., "Large-area synthesis of high-quality and uniform graphene films on copper foils," *Science* **324**(5932), 1312–1314 (2009), http://dx.doi.org/10.1126/science.1171245.

28. X. Li et al., "Transfer of large-area graphene films for high-performance transparent conductive electrodes," *Nano Lett.* **9**(12), 4359–4363 (2009), http://dx.doi.org/10.1021/nl902623y, PMID:19845330.

29. C. Dean et al., "Boron nitride substrates for high-quality graphene electronics," *Nat. Nanotechnnol.* **5**(10), 722–726 (2010), http://dx.doi.org/10.1038/nnano.2010.172.

30. J. Wang et al., "Ultraviolet dielectric hyperlens with layered graphene and boron nitride," *J. Mater. Chem.* **22**(31), 15863–15868 (2012), http://dx.doi.org/10.1039/c2jm32715e.

31. J. J. Miret et al., "Substantial enlargement of angular existence range for dyakonov-like surface waves at semi-infinite metal–dielectric superlattice," *J. Nanophotonics* **6**(1), 063525–063525 (2012), http://dx.doi.org/10.1117/1.JNP.6.063525.

32. K. Novoselov et al., "Electric field effect in atomically thin carbon films," *Science* **306**(5696), 666–669 (2004), http://dx.doi.org/10.1126/science.1102896.

33. V. P. Gusynin, S. G. Sharapov, and J. P. Carbotte, "Sum rules for the optical and hall conductivity in graphene," *Phys. Rev. B* **75**(16), 165407 (2007), http://dx.doi.org/10.1103/PhysRevB.75.165407.

34. G. W. Hanson, "Dyadic green's functions and guided surface waves for a surface conductivity model of graphene," *J. Appl. Phys.* **103**(6), 064302 (2008), http://dx.doi.org/10.1063/1.2891452.

35. D. Pozar, *Microwave Engineering*, John Wiley & Sons, NJ (2009).

36. L. A. Falkovsky and S. S. Pershoguba, "Optical far-infrared properties of a graphene monolayer and multilayer," *Phys. Rev. B* **76**(15), 153410 (2007), http://dx.doi.org/10.1103/PhysRevB.76.153410.

37. L. Hao and L. Sheng, "Optical conductivity of multilayer graphene," *Solid State Commun.* **149**(43), 1962–1966 (2009), http://dx.doi.org/10.1016/j.ssc.2009.07.034.

38. S. Campione et al., "Complex modes and effective refractive index in 3d periodic arrays of plasmonic nanospheres," *Opt. Express* **19**(27), 26027–26043 (2011), http://dx.doi.org/10.1364/OE.19.026027.

39. A. Chebykin et al., "Nonlocal effective parameters of multilayered metal–dielectric metamaterials," *Phys. Rev. B* **86**(11), 115420 (2012), http://dx.doi.org/10.1103/PhysRevB.86.115420.

40. L. Felsen and N. Marcuvitz, *Radiation and Scattering of Waves*, pp. 745–747, IEEE Press, NJ (1994).

41. M. Silveirinha and N. Engheta, "Tunneling of electromagnetic energy through subwave-length channels and bends using ε-near-zero materials," *Phys. Rev. Lett.* **97**(15), 157403 (2006), http://dx.doi.org/10.1103/PhysRevLett.97.157403.

42. B. Edwards et al., "Experimental verification of epsilon-near-zero metamaterial coupling and energy squeezing using a microwave waveguide," *Phys. Rev. Lett.* **100**(3), 033903 (2008), http://dx.doi.org/10.1103/PhysRevLett.100.033903.

43. J. Luo et al., "Oblique total transmissions through epsilon-near-zero metamaterials with hyperbolic dispersions," *Europhys. Lett.* **101**(4), 44001 (2013), http://dx.doi.org/10.1209/0295-5075/101/44001.

44. A. Alu et al., "Epsilon-near-zero metamaterials and electromagnetic sources: tailoring the radiation phase pattern," *Phys. Rev. B* **75**(15), 155410 (2007), http://dx.doi.org/10.1103/PhysRevB.75.155410.

45. S. Campione et al., "Electric field enhancement in epsilon-near-zero slabs under tm-polar-ized oblique incidence," *Phys. Rev. B* **87**(3), 035120 (2013), http://dx.doi.org/10.1103/PhysRevB.87.035120.

46. D. C. Adams et al., "Funneling light through a subwavelength aperture with epsilon-near-zero materials," *Phys. Rev. Lett.* **107**(13), 133901 (2011), http://dx.doi.org/10.1103/PhysRevLett.107.133901.

Mohamed A. K. Othman received a BSc and MSc in electrical engineering from Cairo University, Cairo, Egypt in 2009 and 2012, respectively. During his MSc he worked on modeling of cavity resonators, and he also worked as a researcher in metamaterial-inspired small antenna design for WLAN applications. He is currently a PhD student in Electrical Engineering and Computer Science Department at the University of California, Irvine. His current research interests include metamaterials, plasmonics and terahertz graphene-based devices. He is a student member in SPIE and IEEE.

Caner Guclu received his BS and MS in electrical and electronics engineering from Middle East Technical University, Ankara, Turkey in 2008 and 2010 respectively. During MS, he specialized on RF MEMS-based reconfigurable reflectarray and phased-array antennas as a member of METU MEMS group. He is currently a PhD candidate in Electrical Engineering and Computer Science Department at University of California, Irvine. His recent research interests include characterization of hyperbolic metamaterials, characterization of radiation by isolated sources or by 1-D, 2-D, 3-D arrays of sources in stratified media, silicon-on-insulator optical leaky wave antennas.

Filippo Capolino received the Laurea degree (cum laude) and the PhD degree in electrical engineering from the University of Florence, Italy, in 1993 and 1997, respectively. He is currently an associate professor at the Department of Electrical Engineering and Computer Science of the University of California, Irvine, CA. He has been an assistant professor at the Department of Information Engineering of the University of Siena, Italy. During 1997 to 1999, he was a postdoctoral fellow with the Department of Aerospace and Mechanical Engineering, Boston University, MA. From 2000 to 2001 and in 2006, he was a research assistant visiting professor with the Department of Electrical and Computer Engineering, University of Houston, TX. His research interests include composite metamaterials and their applications, sensors in both microwave and optical ranges, wireless systems, chip-integrated and optical antennas. He has been the EU coordinator of the EU doctoral programs on Metamaterials (2004 to 2009). He is the Editor of the Metamaterials Handbook, CRC Press, 2009.